CrossMark

"Rose Flowers" assembled from mesoporous $NiFe_2O_4$ nanosheets for energy storage devices

Lina Qu[1,2] · Zhoulu Wang[3] · Xianhua Hou[1,2] · Junwei Mao[1,2] · Shaofeng Wang[1,2] ·
Gengzhi Sun[4] · Yuping Wu[3] · Xiang Liu[3,4]

Abstract Rose flower-like $NiFe_2O_4$ composite, uniformly distributed on 3D Ni foam substrate, is successfully prepared via a facile, cost-effective hydrothermal growth process followed by sintering. The structure of the sample is tested by X-ray diffraction while the morphology is characterized by scanning electron microscopy and transmission electron microscopy. The flower-like $NiFe_2O_4$ materials are applied as potential anode for lithium-ion batteries (LIBs) which have the highest energy density and play enssential role for the electronic vehicles and sodium ion batteries (SIBs) which are candidates for replacing LIBs because of the abundant nature storage. Electrochemical results confirmed that the anode exhibits good cycling performance with a stable specific capacity and rate capability both in LIBs and SIBs. Furthermore, the cycling performance for LIBs is demonstrated to be 1126 mAh g^{-1} even after 100 cycles while the Na storage behavior of rose flower-like $NiFe_2O_4$ materials as an anode material for SIBs is essentially investigated. It exhibits a high original discharge capacity of 584 mAh g^{-1}, and steady capacity retention of 304 mAh g^{-1} after 100 cycles. Moreover, the long cycle capacity expressed to be ~250 mAh g^{-1} even after 1300 cycles suggests a good cycling performance in this report for SIBs.

1 Introduction

Lithium-ion batteries (LIBs) and sodium-ion batteries (SIBs) have attracted enormous interest as potential candidates for the next-generation energy storage systems for portable devices and transportation applications [1–4]. Therein the development of LIBs has beening mature along with continuous improving of charge/discharge rates and service safety due to its low self discharge, higher energy density, environmental friendliness and long lifespan [5–7]. And it also shows great practical application but is limited by the shortage of Lithium resource. To meet the increasing need, the sodium which possesses larger reserves and relatively low working potential have also been the research hotspot for many people. Both devices share similar electrochemical mechanism accompanying the intercalation/de-intercalation of metal ions (Li^+ or Na^+) into/from anodes during charge–discharge process [8, 9]. This process normally results in the lattice expansion/contraction, particularly for SIBs because of the larger radius (0.102 nm) of Na ion than that (0.076 nm) of Li ion [10–14]. Therefore, the design of active materials with tunable sizes, especially mesoporous structure (2–100 nm), would be better and beneficial for the diffusion of both Li^+ and Na^+ on account of smaller structure perturbation [15–17].

✉ Xianhua Hou
  houxianhua@m.scnu.edu.cn

✉ Xiang Liu
  iamxliu@njtech.edu.cn

1 Guangdong Engineering Technology Research Center of Efficient Green Energy and Environment Protection Materials, Guangzhou 510006, People's Republic of China

2 Guangdong Provincial Key Laboratory of Quantum Engineering and Quantum Materials, School of Physics and Telecommunication Engineering, South China Normal University, Guangzhou 510006, People's Republic of China

3 School of Energy Science and Engineering, Nanjing Tech University, Nanjing 210009, People's Republic of China

4 Key Laboratory of Flexible Electronics (KLOFE) & Institute of Advanced Materials (IAM), Jiangsu National Synergistic Innovation Center for Advanced Materials (SICAM), Nanjing Tech University (NanjingTech), Nanjing 211816, People's Republic of China

Considering the similar electrochemical mechanism of LIBs and SIBs, graphite is often applied as commercial electrode material in many LIBs and SIBs. However, the relatively low theoretical specific capacity and low intercalated-Li potential of graphite limit the further development of LIBs [18, 19]. In case of NIBs, the intercalation of Na^+ in commercial graphite is more difficult because of the larger radius of Na^+ [20–23]. Therefore, developing new anode materials with appropriate electrode potential, higher energy density and lasting safety as substitutes for graphite becomes the key to improve the performance of LIBs and SIBs. Newly, oxides specially with spinel structure (AB_2O_4, A = Ni, Zn, Co, Fe or Mn; B = Fe, Ni, Co, Mn or Zn; A ≠ B) essentially have been employed as hopeful anode electrode materials for both LIBs and SIBs owing to the comparatively appropriate working voltage as well as high theoretical specific capacities (~500–1000 mAh g^{-1}) [24–26]. Among them, $NiFe_2O_4$ (NFO) have attracted considerable interest as anode materials for LIBs and SIBs for its high theoretical capacity, natural abundance and low cost [27, 28]. Unfortunately, the utilization of NFO in LIBs and SIBs is vitally limited by its low conductivity and drastic volume changes during ion insertion and extraction process, therefore seriously deteriorating its electrochemical performances [29–31]. Many efforts, such as elements doping, morphological optimization and carbon coating, have been made to solve the aforementioned problems [32–35]. Generally, anode materials with self-assembled hierarchical achitecture based on 3D conductive alloy-matrix can not only enhance the electrical conductivity of the anode materials but also offer a larger surface area and avoid the "dead surface" compared with traditional slurry-based electrodes. Besides, the design of 3D structured electrode allows for more efficient electron- and ion-transfer, and enhances the structure stability during charge–discharge cycles by accommodating volume changes, which may be beneficial to improve the electrochemical performance of LIBs and SIBs [21, 36, 37]. Moreover, the 3D monolithic electrode could be straight applied as conductive- and binder- agent-free electrodes, hence avoiding the intricate experimental procedures [38, 39]. Therefore, it can be envisioned that the construction of NFO-based anode materials with hierarchical architectures on 3D conductive metallic substrate would be a promising strategy for the preparation of higher performance anodic electrode in energy storage devices.

Herein, we report a design of freestanding rose flower-like hierarchical structure assembled from mesoporous NFO nanosheets on 3D Ni foam via a convenient, low cost hydrothermal method followed by sintering. The obtained monolithic electrode was applied as the conductive- and binder-agent-free anode materials for LIBs and SIBs.

2 Experimental

2.1 Synthesis of the monolithic anodic electrode

All chemicals (analytical grade) were purchased from Sigma-Aldrich with none other purification. In a typical synthesis process as shown in scheme 1. $Ni(NO_3)_2·6H_2O$ (2 mmol) and $ZnSO_4·7H_2O$ (4 mmol) were poured into deionized water (100 mL), mixing and stirring, to form a homogeneous dark yellow solution, thereafter with the addition urea (4 mmol) and NH_4F (2 mmol). Prior to deposition, a piece of 3D Ni foam (4×6 cm) was ultrasonically cleaned for 15 min in acetone, 20 min in 1 M HCl solution, 30 min in deionized water and 30 min in ethanol, respectively. Then the pretreated 3D Ni foam
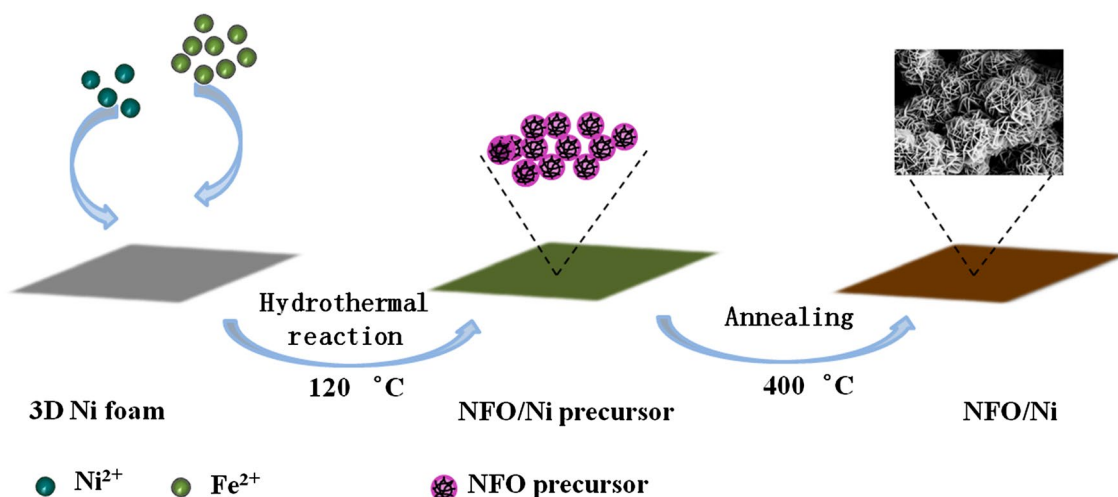
Scheme 1 The facile preperation of the as-prepared flower-like NFO growing on 3D Ni foam

and the well dispersed solution were transferred into a Teflon-lined stainless steel autoclave (150 mL in volume) and heated at 120 °C for 10 h. After the autoclave cooled down naturally to room temperature. The final product was washed several times and vacuum dried, then underwent heat treatment at 400 °C in argon for 2 h to obtain rose flower-like hierarchical structure assembled from NFO nanosheets on 3D Ni foam (NFO/Ni).

2.2 Characterizations

The structures of the samples were characterized by X-ray diffraction system (XRD, PANalytical X'pert PRO, Cu/K$_\alpha$ radiation, $\lambda = 1.5406$ nm) with Cu/K radiation ($\lambda = 1.5406$ nm), X-ray photoelectron spectroscopy (XPS, ESCALAB 250 with 150 W Al Ka probe beam) and N$_2$ adsorption/desorption with a Coulter SA 3100 surface area analyzer. And the morphology was presented through scanning electron microscope (SEM, ZEISSUL-TRA55) and transmission electron microscope (TEM, JEM-2100).

2.3 Battery assembly and electrochemical measurements

Electrochemical experiments were performed by using half-cells (CR 2430) with Celgard 2400 as a separator and lithium-foil/sodium-foil as a counter electrode, respectively. NFO/Ni was cut into pallets with a diameter of 16 mm and used as a working electrode directly without any conductive additive or polymeric binder. The loading amount of the NFO were calculated to be 1.0 mg cm^{-2}. For LIBs, the electrolyte was 1 M LiPF$_6$ dissolved in diethyl carbonate (DEC), ethyl carbonate (EC) and dimethyl carbonate (DMC) (1:1:1 by volume). For SIBs, the electrolyte was 1 M NaClO$_4$ with the existing of Ec and DEC (1:1 by volume), as well as the addition of 5% fluoroethylene carbonate (FEC). Ultimately, the whole half-cells were assembled in glove box filled with argon. The galvanostatic charge and discharge experiments were performed using a battery tester (LAND-CT2001A) within a voltage window of 0.01–3.00 V at the room temperature. Cyclic voltammetry (CV) measurements were carried out by using an electrochemical workstation (1470E, Solartron Analytical) at a scan rate of 0.2 mV s^{-1} in a voltage range from 0.01 to 3.00 V. The electrochemical impedance spectroscopy (EIS) measurements were tested within a frequency range of 100 kHz–0.01 Hz on a solartron analytical electrochemical workstation.

3 Results and discussion

3.1 Structural and morphological characterization

Typical XRD pattern of the as-synthesized NFO on 3D Ni foam after heat treatment is shown in Fig. 1. Apart from two strong peaks originating from Ni foam substrate at approximately 44.5° and 51.9° (JCPDS: 04-0850), the other diffraction peaks could be indexed to the spinel NFO phase (JCPDS 10-0325) without any impurity, showing the completely growth of NFO on the surface of 3D Ni foam. The sharp peaks also indicate that the as-prepared NFO has a good crystallinity.

The morphology and microstructure of NFO grown on 3D Ni foam is examined by SEM (Fig. 2). The as-prepared NFO with an uniform morphology is successfully loaded on the 3D Ni foam surface (Fig. 2a). The magnified SEM images shown in Fig. 2b, c indicate that the sample composes of abundant rose flower-like NFO with a diameter of ~2 μm homogeneous distributed on the the 3D Ni foam network. The rose flower-like hierarchical structure is assembled from many ultrathin NFO nanosheets with plenty of mesoporous which immensely increase the specific surface area of anode materials thus is helpful for fast ion (Li$^+$ or Na$^+$) transportation (Fig. 2d). And Fig. 2e expounds the Li$^+$ intercalation schematic of the active materials during the diacharge process. The nanosheets of the flower-like NFO would generally expand and be thickened when a lot of Li$^+$/Na$^+$ are embedded. Yet this behavior would not be able to destory the integrity of active materials NFO benefiting from the good self-assembly architecture as shown in Fig. 2a–d, and the petals space between the nanosheets provides effective buffer space to adapt to the volume expansion.

The detailed microstructure of the synthesized NFO can be attained from the transmission electron microscopy (TEM) images in Fig. 3. The image of low magnification (Fig. 3a) implies that the nanosheets are incessant with coarse surfaces in which numerous interconnected
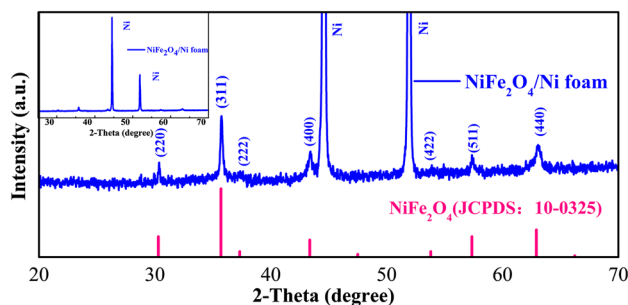

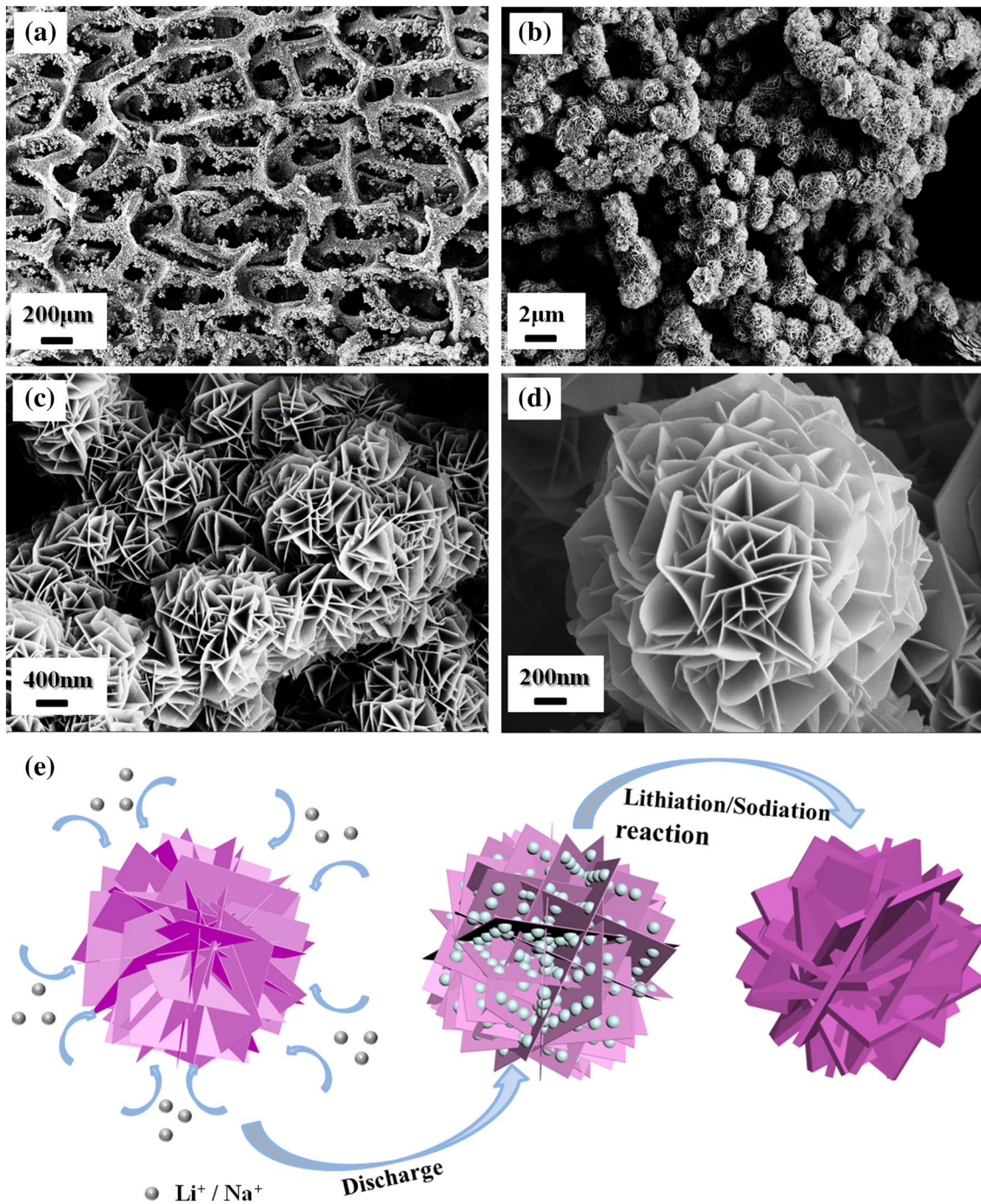**Fig. 1** XRD patterns of the as-synthesized NFO developed on 3D Ni foam

Fig. 2 a SEM image of the NFO/Ni. **b–d** SEM iamges of rose flower-like nanostructures assembled from NFO nanosheets on 3D Ni foam at different magnification. **e** The Li$^+$ intercalation schematic of the active materials

nanoparticles assembled into sheet-like structures. The magnified image (Fig. 3b) clearly shows that the pores are distributed evenly throughout the surface of the each single nanosheet. The formation of the pores in the nanosheets may be involved to the liberation of gases during thermal treatment as a result of the decomposition of the precursors [37]. The resolved lattice fringe shown in Fig. 3c is about 0.25 and 0.16 nm, which could be assigned to the (311) and (511) planes of the NFO phase. This result further confirms the formation of crystalline NFO and has a consistency with the XRD pattern (Fig. 1). In addition, the matching selected area electron diffraction (SAED) pattern (Fig. 3d) displays clearly incontinuous diffraction waves indicating the polycrystal
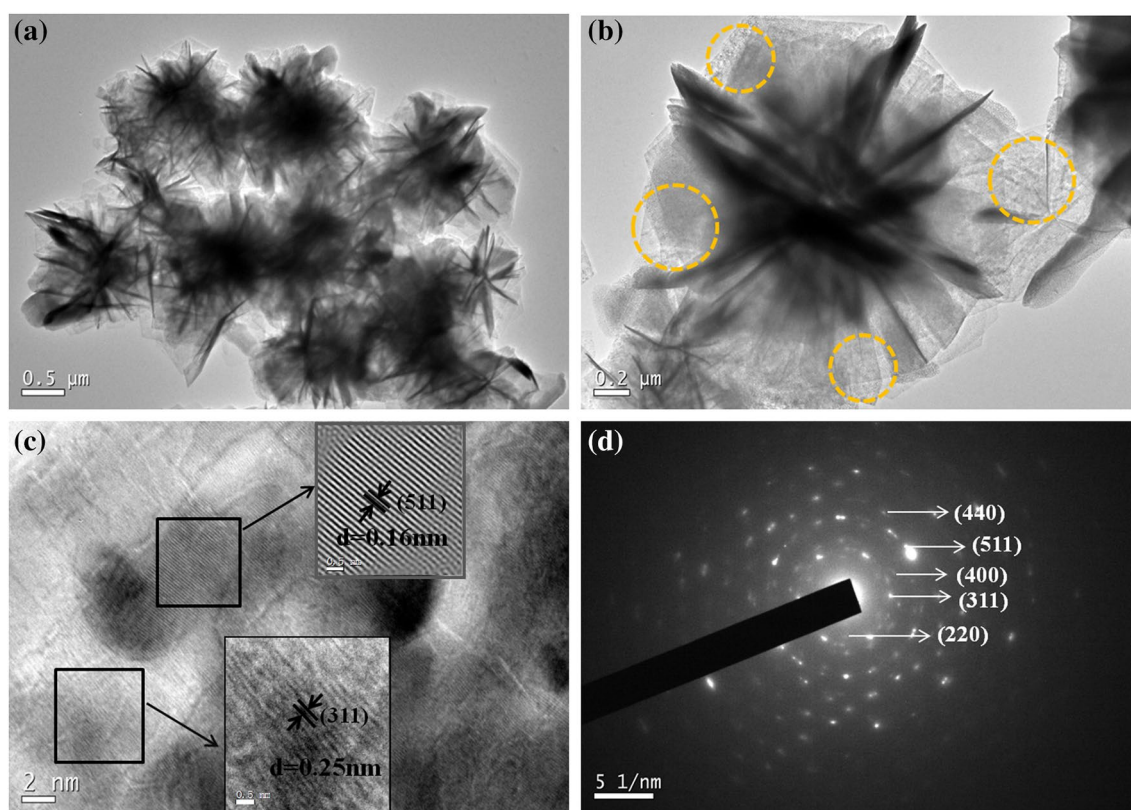
Fig. 3 **a, b** TEM images, **c** HRTEM image and **d** SAED pattern of the rose flower-like NFO scratched down from the 3D Ni foam

character of the nanosheets. The diffraction rings matched with (220), (311), (400) of NiO phase while the diffraction rings of (511) and (440) correspond to the planes of Fe_2O_3 phase [40].

X-ray photoelectron spectroscopy (XPS) was applied to identify the chemical valence states of each elements in NFO In Fig. 4a, the two principal peaks located at the binding energy of 855.6 and 873.7 eV are contributed to Ni $2p_{3/2}$ and Ni $2p_{1/2}$. Two satellite peaks (identified as "sat.") at the binding energy of 870.6 and 862.3 eV indicate the coexistence of Ni^{2+} and Ni^{3+}, which is conducive to the electron transfer during the charge/discharge process [41]. In Fig. 4b, the peaks centered at 710.8 and 712.1 eV are fitted to tetrahedral (A-site) and octahedral (B-site), respectively, which can be assigned to Fe $2p_{3/2}$ [42, 43]. The other peaks at binding energy of 717.9 and 724.7 eV correspond well to the shake-up satellite structure and the Fe $2p_{1/2}$, respectively, suggesting the presence of Fe(III) in the NFO [25]. Figure 4c shows two sharp peaks of O 1s located at the binding energy of 531.3 and 529.7 eV. The former might be attributed to the metal–oxygen bond [44, 45], while the latter may be ascribed to the defects, inevitable contaminants or some surface species, such as chemisorbed oxygen, hydroxyls, or species intrinsic to the spinel surface [46, 47].

The specific surface area and pore size distribution of NFO is determined by N_2 adsorption/desorption isothems as shown in Fig. 4d. The hysteresis loop with the region at P/P_0 of 0.6–1.0, which could be indexed to be the H3 type on the basis of IUPAC classification, suggests the existance of micropores and mesoporous in the NFO. This result is in accord with the observation result in TEM. The specific surface area calculated by Brunauer–Emmett–Teller (BET) method is 99.6 m^2 g^{-1}. Such a large surface area is beneficial to the efficient utilization of active materials, thus offers high specific capacitance. In addition, the pore size distribution analysis is analyzed using Barrett–Joyner–Halenda (BJH) method (Fig. 4d). The pore size of NFO mostly falls in range between 2 and 5 nm corresponding to the mesoporous structure. This mesoporous structure may provide a quick access for Li^+/Na^+ diffusion during the insertion/extraction processes, which is well expected to improve the electrochemical performance of LIBs and SIBs.

3.2 Lithium storage performance

In order to evaluate the electrochemical performance of the as-synthesized the NFO/Ni anodes in LIBs, the samples are firstly assembled into CR2430 coin cells using lithium foil
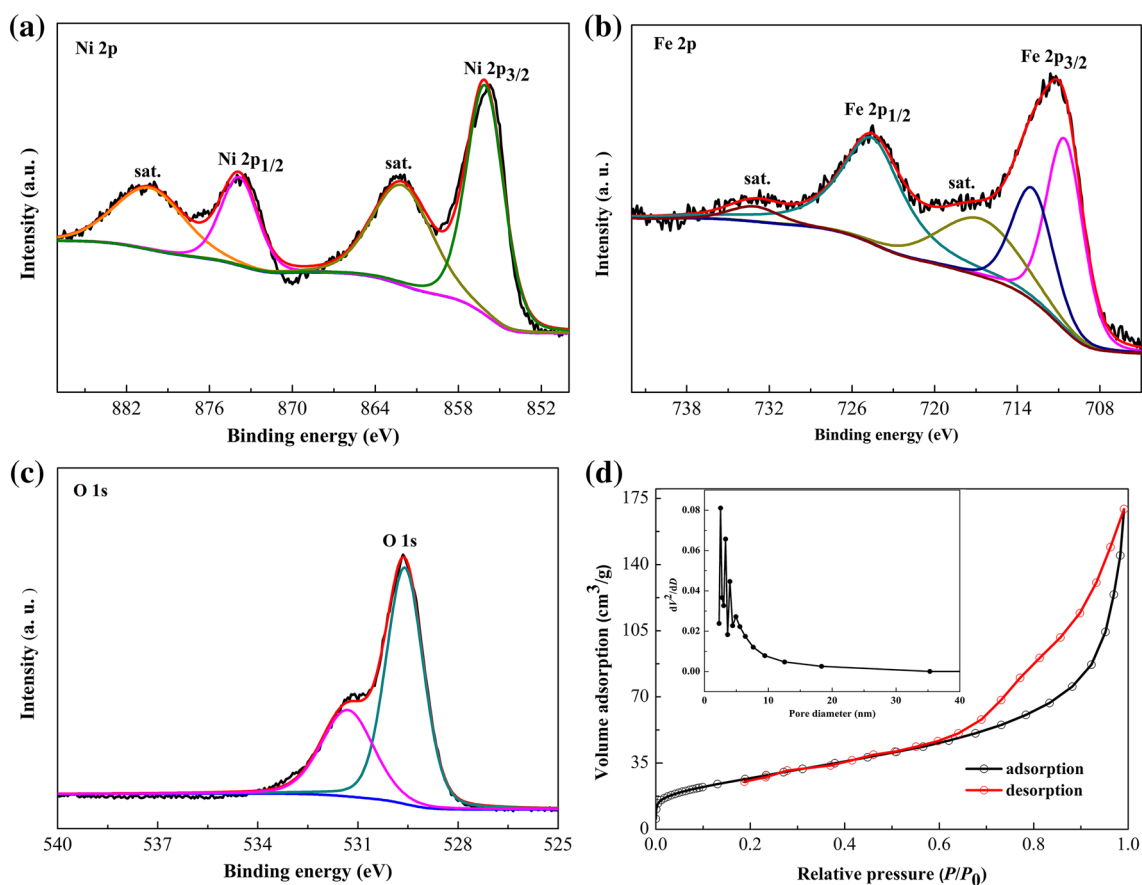
Fig. 4 XPS spectra of **a** Ni 2p, **b** Fe 2p and **c** O 1s. **d** N_2 adsorption/desorption isothems and the corresponding pore size distribution (*inset*) of $NiFe_2O_4$ scratched down from the 3D Ni foam

as the reference. The cyclic voltammograms (CVs) of the electrode are recorded for the first five cycles at a scan rate of 0.2 mV s^{-1} with the voltage range of 0.01–3.00 V shown in Fig. 5a. During the first sweep, the cathodic peak of the NFO/Ni is located at 0.51 V which can be ascribed to the reduction of the cations to their metallic status ($Fe^{3+} \rightarrow Fe^0$, $Ni^{2+} \rightarrow Ni^0$) and the formation of solid electrolyte interphase (SEI) films resulting from the decomposition of electrolyte [48]. The broad anodic peak located at about 1.73 V corresponds to the oxidation of metallic Ni and Fe to their metal oxides, respectively. In subsequent cycles, the cathodic peak at 0.78 V and the anodic peak at 2.01 V could be attributed to the reversible redox reaction of Ni^{2+}/Ni^0 and Fe^{3+}/Fe^0, respectively during the charge–discharge cycle [49]. Furthermore, the position of cathodic/anodic peaks remain unchanged since the 2nd cycle, implying good reversibility of the electrochemical reactions [50].

The galvanostatic charge–discharge voltage profiles for the 1st, 2nd, 50th and 100th cycle of the NFO@Ni electrode are investigated at a current density of 100 mA g^{-1}. As shown in Fig. 5b, the premier charge and discharge capacities are 1168 and 1500 mAh g^{-1}, respectively, with

a coulombic efficiency (CE) of 77.9%. The capacity loss in the initial cycle could derive from the irreversible growing of SEI films and the Li_2O formation during the reduction of metal oxide, which is normally ascribed to various metal oxides electrodes [51]. In the second cycle, the NFO/Ni electrode displays high charge and discharge capacities of 1208 and 1236 mAh g^{-1}, respectively, with a high CE of 97.7%. After charge–discharge for 100 cycles, the electrode exhibits a discharge capacity of 1109 mAh g^{-1}, which is approximately 94.9% of the initial value.

In Fig. 5c, the cycling performance and CE of the NFO/Ni electrode are tested with current density of 100 mA g^{-1}. The capacity of the NFO/Ni electrode slowly decreases to 1095 mAh g^{-1} in the original 22 cycles, then maintains at 1120 mAh g^{-1}. The slight increase in capacity after the 22th cycle is mainly attributed to the electrolyte penetration and materials activation [52]. After 100 cycles, the anode shows a high discharge capability of 1126 mAh g^{-1}. Compared with the previous reports, one-dimensional nanotube structure discovered by Wang et al. [42]. and nanoparticles researched by Fu et al. [53]., the high capacity and excellent cycling stability of NFO/Ni anode in this report
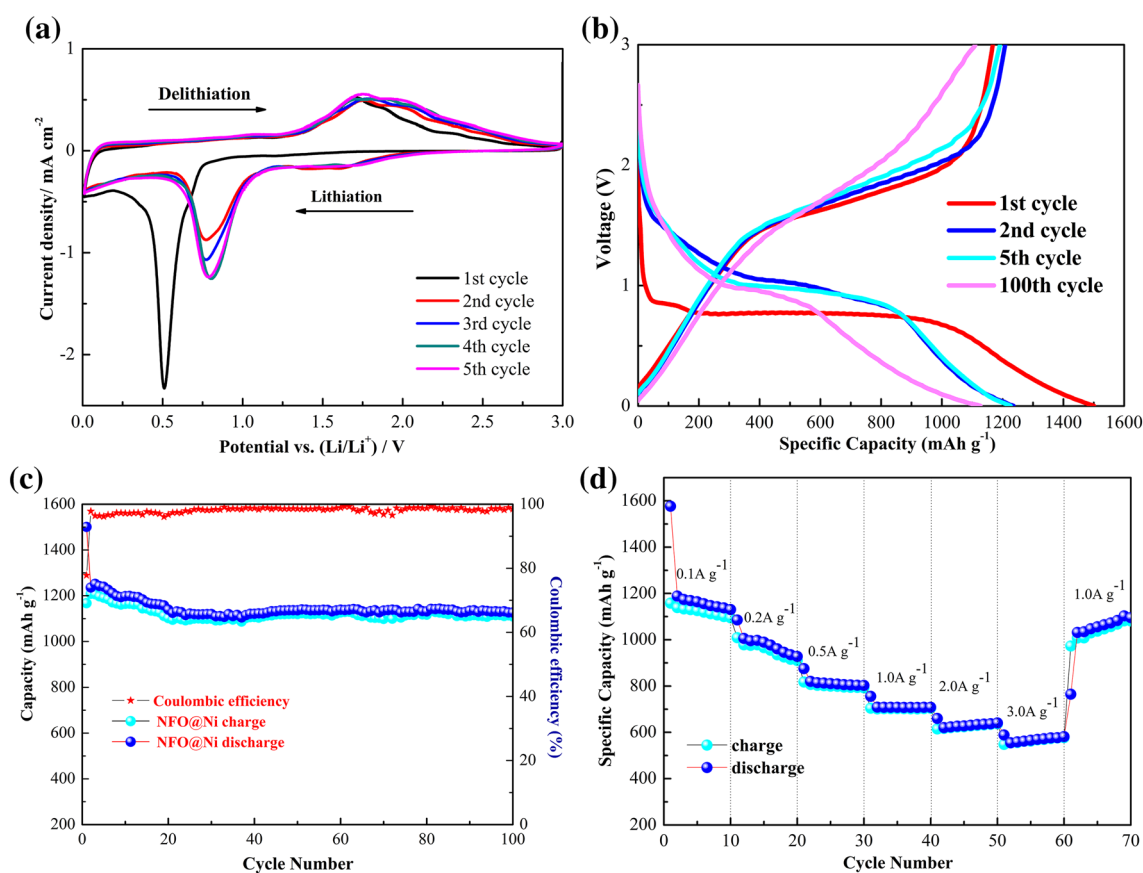
Fig. 5 **a** Cyclic voltammetry curves of NFO/Ni at a scan rate of 0.2 mV s^{-1}, **b** galvanostatic charge–discharge profiles of NFO/Ni with voltage range of 0.01–3 V versus Li/Li$^+$ and current density of 100 mA g^{-1}, **c** cycling performance of NFO/Ni at a current density of 100 mA g^{-1} for 100 cycles, **d** rate performance of NFO/Ni at different current densities

can be ascribed to the novel rose flower-like architectures assembled from mesoporous NFO nanosheets which not only could shorten the diffusion length of Li$^+$ and electrons, thus improving the kinetic properties, but also reduce the volume expansion effect during the charge–discharge processes.

The rate performance is evaluated at kinds of current densities ranging from 0.1 to 3.0 A g^{-1} shown in Fig. 5d. It can be seen that the charge capacity slightly reduces from 1157 mAh g^{-1} at a current density of 0.1 A g^{-1} to 915, 793, 701, 614, 555 mAh g^{-1} at current densities of 0.2, 0.5, 1.0, 2.0, 3.0 A g^{-1}, respectively. Remarkably, the capacity of 1008 mAh g^{-1} is still retained when the current density changes from 3.0 back to 0.1 A g^{-1}. At the last cycle, the capacity retention is 94.6%, suggesting the excellent rate performance of the NFO/Ni anode for LIBs.

Electrochemical impedance spectroscopy (EIS) is a useful analytical means to analyze the kinetics of the as-prepared electrodes [54, 55]. As shown in Fig. 6b, EIS measurements are performed during the 1st and 2nd charge–discharge process under specific voltages at the point from a to j (displayed in Fig. 6a). The results are

presented as Nyquist plots (*Zre vs. Zim*) in Fig. 6b with the real parts (*Zre*) and imaginary parts (*Zim*) of the cell impedance, respectively. In the Nyquist plots, the intercept of the semicircle at high frequency is the ohmic resistance (R_e) which is an indication of the series impedence of the cell. The value of R_e is ~1.6 Ω. At the open circuit voltage (1.68 V), only a semicircle is observed in an impedance of ~64 Ω from the high to the medium frequency. It could be ascribed to the surface film (R_{sf}), charge transfer resistance (R_{ct}) and the relative capacitance (CPE_1) [56]. During the next discharge process, another semicircle, appearing in low frequency range, is attributed to the bulk resistance (R_b) and the related constant phase element is CPE_2. The value of $R_{sf}+R_{ct}$ gradually decreases during the discharge (lithiation) process while the R_b remains unchanged. Besides, the value of $R_{sf}+R_{ct}$ increases at the high-to-medium frequency and the semicircle at low frequency namely R_b no longer appears during the charge (delithiation) process. Moreover, the observed impedances at discharge voltage plateau and charge voltage plateau during the 2nd cycle present a similar plot state and close resistance value with the 1st cycle, displaying a optimization of
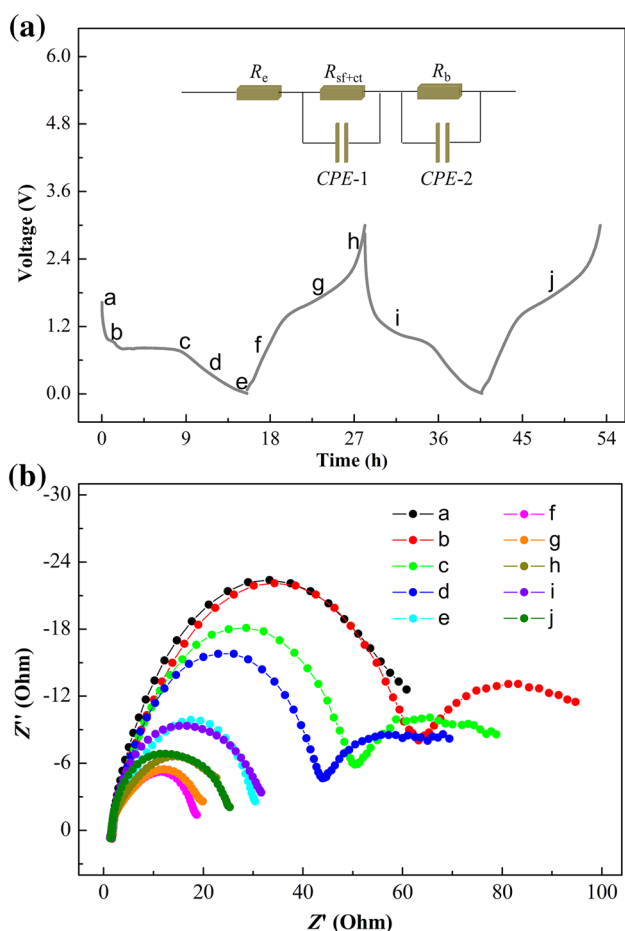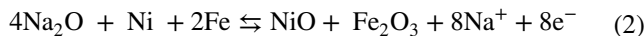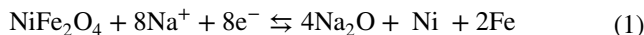
(a)

(b)

Fig. 6 a Galvanostatic charge–discharge profiles of NFO/Ni with voltage range of 0.01–3.00 V versus Li/Li$^+$ and current density of 100 mA g^{-1}. And the equivalent electrical circuit for the observed Nyquist plots in the *inset*. **b** The corresponding Nyquist plots (Z′ vs. Z″) of the as-prepared electrode materials at various voltages during the first two cycles

electronic conductivity for the active material and good ion conductivity for the electrolyte spread all over the pores of the electrode composites [57, 58].

3.3 Sodium storage performance

SIBs based on NFO/Ni are also devised using sodium foil as the reference electrode. The CV curves during the voltage range of 0.01–3.00 V with a scan rate of 0.20 mV s^{-1} (vs. Na/Na$^+$) are shown in Fig. 7a. A broad cathodic peak locates at 0.35 V in the first cycle is found, corresponding to the reduction reaction of NFO to metallic iron (Fe) and nickel (Ni) and the electrochemical formation of Na$_2$O, accompanied with the growing of SEI film. The position of this cathodic peak is lower than that for LIBs, implying a slower reaction kinetics in SIBs due to the larger ionic radius of Na$^+$ [59]. In the following cycles, the cathodic

peak shifts to 0.65 V. On the other hand, the anodic peak in the vicinity of 1.70 V in the initial five cycles corresponds to the oxidation reaction of Fe^0→Fe^{3+}, Ni^0→Ni^{2+} and decomposition of Na$_2$O. The conversion reaction mechanism of NFO with Na may be depicted as following steps, which has been verified in other metal oxides in previous studies [13]:

$$NiFe_2O_4 + 8Na^+ + 8e^- \leftrightarrows 4Na_2O + Ni + 2Fe \quad (1)$$

$$4Na_2O + Ni + 2Fe \leftrightarrows NiO + Fe_2O_3 + 8Na^+ + 8e^- \quad (2)$$

The galvanostatic charge–discharge profiles of SIBs during the potential range of 0.01–3.00 V with a current density of 100 mA g^{-1} are shown in Fig. 7b. The initial charge and discharge capacities reach 346 and 584 mAh g^{-1}, respectively, with a moderate initial CE of 59%. Compared with LIBs, the larger irreversible loss and the lower initial CE for Na-storage is probably caused by the thick SEI films formed on the surface of NFO during the first sodiation process and the part volume changes deriving from the insertion of Na$^+$ which posseses larger size [60]. After five cycles, when electrode is fully infiltrated by electrolyte, CEs significantly improve to above 90%. After 100 cycles, the electrode exhibits a reversible discharge capacity of 304 mAh g^{-1} with a high CE of 98%. The cycling performance of the cells at a current density of 100 mA g^{-1} is shown in Fig. 7c. The columbic efficiency of the anode increases continuously along with cycling, lastly reaching around 98%. And the specific capacity maintains 304 mAh g^{-1} even after 100 cycles at 100 mA g^{-1} with a specific capacity retention of 52%. Moreover, the long cycling with current density of 50 mA g^{-1} in Fig. 7e also shows a stable cycle performance which possesses ~250 mAh g^{-1} even after 1300 cycles. The capacity fading might be mostly due to the large volume change during the sodiation and desodiation reaction processes. Compared to other anode electrode materials for SIBs, such as hollow NiCo$_2$O$_4$ nanoboxes [61], bowl-like hollow Co$_3$O$_4$ microspheres [62], the NFO/Ni anode in this study displays higher reversible capacity and cycling stability, suggesting that NFO/Ni is a promising anode candidate for SIBs.

The rate performance is an important indicator for practical applications. The consecutive cycling performance of the cells at different charge–discharge current densities from 0.1 to 3.0 A g^{-1} are shown in Fig. 7d The reversible capacities are 356.5, 340.3, 319.3, 382.2, 246.6 and 178.9 mAh g^{-1} at 0.1, 0.2, 0.5, 1.0, 2.0 and 3.0 A g^{-1} respectively. Remarkably, even at a high current density of 3.0 A g^{-1}, the capacity could still maintain 178.9 mAh g^{-1}, much higher than that of the carbon materials among the previously reported anode materials commonly used for SIBs [63, 64]. The better cyclic stability along with excellent rate performance could be
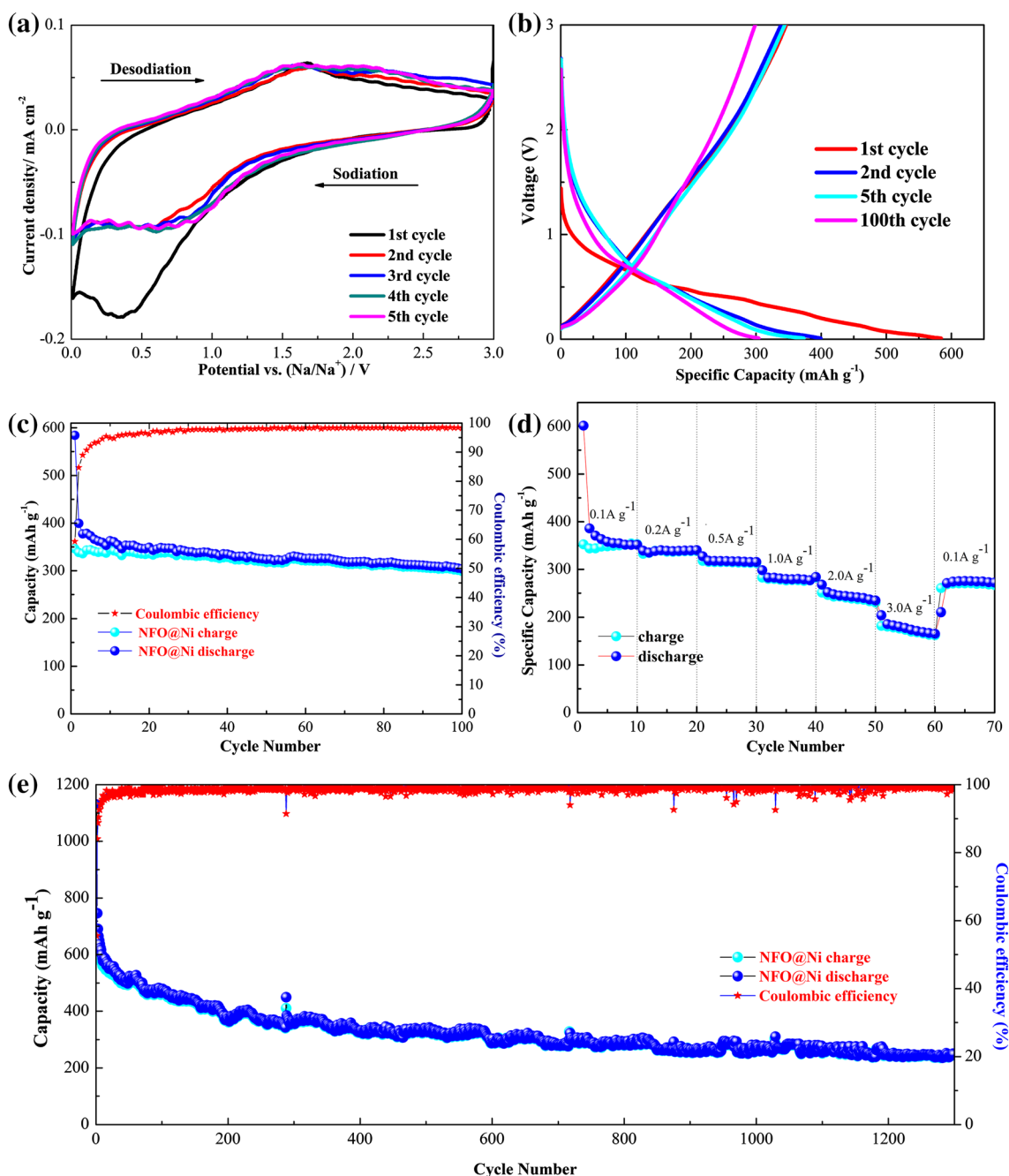
Fig. 7 a Cyclic voltammetry curves of NFO/Ni at a scan rate of 0.20 mV s^{-1}, **b** galvanostatic charge–discharge profiles of NFO/Ni with voltage range of 0.01–3.00 V versus Na/Na$^+$ at current density of 100 mA g^{-1}, **c** cycling performance of NFO/Ni at a current density of 100 mA g^{-1} for 100 cycles, **d** rate performance of NFO@Ni at different current densities. **e** Cycling peformance of NFO@Ni at a current density of 50 mA g^{-1} for 1300 cycles

assigned to the special hierarchical mesoporous structure of the NFO/Ni which can relieve the volume expansion and provide rich pathways of Na$^+$ inserting and extracting.

4 Conclusions

In summary, a rose flower-like structure assembled from numerous mesoporous NFO nanosheets on 3D Ni foam

is successfully prepared through a facile, environmentally friendly and cost-effective hydrothermal growth followed by sintering. Owing to the higher specific surface area and unique porous flower-like structure, the anode electrode based on NFO/Ni exhibits excellent electrochemical performances for both LIBs and SIBs, proved to be in two main aspects. The cycling performances are improved to be more stable and higher capacity retention with a high specific capacity of 1126 mAh g^{-1} after 100 cycles for LIBs and ~250 mAh g^{-1} even after 1300 cycles for SIBs. In addition, the rate performances is also showed superiorly in that the specific capacity still remains higher at high current densities for both LIBs and SIBs. These results demonstrate advantages of the NFO/Ni as a promising anode candidate both for LIBs/SIBs. This strategy generally extends the possibility to design and fabricate all other 3D transition metal oxides electrode materials, which are widely used for potential applications in catalytic, electronic, and energy storage systems.

References

1. D.Q. Zhu, F.C. Zheng, S.H. Xu, Y.G. Zhang, Q.W. Chen, Dalton Trans **44**, 16946–16952 (2015)
2. Y.C. Dong, K.C. Yung, R.G. Ma, X. Yang, Y.S. Chui, J.M. Lee, J.A. Zapien, Carbon **86**, 310–317 (2015)
3. J.F. Wu, Y.H. Song, R.H. Zhou, S.H. Chen, L. Zuo, H.Q. Hou, L. Wang, J. Mater. Chem. A **3**, 7793–7798 (2015)
4. Q.T. Qu, T. Gao, H.Y. Zheng, X.X. Li, H.M. Liu, M. Shen, J. Shao, H.H. Zheng, Carbon **92**, 119–125 (2015)
5. N. Atar, T. Eren, M.L. Yola, H. Gerengi, S.B. Wang, Ionics **21**, 3185–3192 (2015)
6. N. Atar, T. Eren, M.L. Yola, Thin Solid Films **590**, 156–162 (2015)
7. N. Atar, T. Eren, M.L. Yola, H.K. Maleh, A.T. Çolak, A. Olgun, Ionics **21**, 2193–2199 (2015)
8. L. Bodenes, A. Darwiche, L. Monconduit, H. Martinez, J. Power Sources **273**, 14–24 (2015)
9. I. Elizabeth, B.P. Singh, S. Trikha, S. Gopukumar, J. Power Sources **329**, 412–421 (2016)
10. Y.H. Xu, Y.J. Zhu, Y.H. Liu, C.S. Wang, Adv. Energy Mater. **3**, 128–133 (2013)
11. L.F. Xiao, Y.L. Cao, J. Xiao, W. Wang, L. Kovarik, Z. Niea, J. Liu, Chem. Commun. **48**, 3321–3323 (2012)
12. N. Yabuuchi, K. Kubota, M. Dahbi, S. Komaba, Chem. Rev. **114**, 11636–11682 (2014)
13. Y.D. Mo, Q. Ru, J.F. Chen, X. Song, L.Y. Guo, S.J. Hu, S.M. Peng, J. Mater. Chem. A **3**, 19765–19773 (2015)
14. S.M. Oh, S.T. Myung, C.S. Yoon, J. Lu, J. Hassoun, B. Scrosati, K. Amine, Y.K. Sun, Nano Lett. **14**, 1620–1626 (2014)
15. F. Zou, Y.M. Chen, K. Liu, Z. Yu, W.F. Liang, S.M. Bhaway, M. Gao, Y. Zhu, ACS Nano. **10**, 377–386 (2016)
16. D.L. Chao, C.G. Zhu, P.H. Yang, X.H. Xia, J.L. Liu, J. Wang, X.F. Fan, S.V. Savilov, J.Y. Lin, H.J. Fan, Z.X. Shen, Nat. Commun. (2016) doi:10.1038/ncomms12122.
17. B. Luo, T.F. Qiu, D.L. Ye, L.Z. Wang, L.J. Zhi, Nano. Energy **22**, 232–240 (2016)
18. Z.A. Zhang, X.X. Zhao, J. Li, Electrochim. Acta **176**, 1296–1301 (2015)
19. R.R. Gaddam, D.F. Yang, R. Narayan, K. Raju, N.A. Kumar, S.X. Zhao, Nano Energy **26**, 346–352 (2016)
20. C.Z. Yuan, H. Cao, S.Q. Zhu, H. Hua, L.R. Hou, J. Mater. Chem. A **3**, 20389–20398 (2015)
21. Z.Q. Li, L.W. Yin, J. Mater. Chem. A **3**, 21569–21577 (2015)
22. X.Y. Qin, H.R. Zhang, J.X. Wu, X.D. Chu, Y.B. He, C.P. Han, C. Miao, S. Wang, B.H. Li, F.Y. Kang, Carbon **87**, 347–356 (2015)
23. S.H. Park, W.J. Lee, Carbon **89**, 197–207 (2015)
24. C.T. Cherian, J. Sundaramurthy, M.V. Reddy, P.S. Kumar, K. Mani, D. Pliszka, C.H. Sow, S. Ramakrishna, B.V.R. Chowdari, ACS Appl. Mater. Interfaces **5**, 9957–9963 (2013)
25. L.R. Hou, L. Lian, L.H. Zhang, G. Pang, C.Z. Yuan, X.G. Zhang, Adv. Funct. Mater. **25**, 238–246 (2015)
26. M.V. Reddy, C.Y. Quan, K.W. Teo, L.J. Ho, B.V.R. Chowdari, J. Phys. Chem. C **119**, 4709–4718 (2015)
27. Y. Xia, B. B. Wang, G. Wang, X. J. Liu, H. Wang, ChemElectroChem **3**, 299–308 (2016)
28. G.D. Park, J.S. Cho, Y.C. Kang, ACS Appl. Mater. Interfaces **7**, 16842–16849 (2015)
29. E.K. Heidari, B. Zhang, M.H. Sohi, A. Ataieb, J.K. Kim, J. Mater. Chem. A **2**, 8314–8322 (2014)
30. M. Fu, Q.Z. Jiao, Y. Zhao, J. Mater. Chem. A **1**, 5577–5586 (2013)
31. G. Huang, F.F. Zhang, L.L. Zhang, X.C. Du, J.W. Wang, L.M. Wang, J. Mater. Chem. A **2**, 8048–8053 (2014)
32. J.W. Mao, X.H. Hou, F.S. Huang, K.X. Shen, K.H. Lam, Q. Ru, S.J. Hu, J. Alloys Comp. **676**, 265–274 (2016)
33. L. Liu, L.M. Sun, J. Liu, X.L. Xiao, Z.B. Hu, X.Z. Cao, B.Y. Wang, X.F. Liu, Int. J. Hydrogen Energy **39**, 11258–11266 (2014)
34. L. Luo, R.R. Cui, K. Liu, H. Qiao, Q.F. Wei, Ionics, **21**, 687–694 (2015)
35. Y.D. Ma, X.P. Dai, M.Z. Liu, J.X. Yong, H.Y. Qiao, A. Jin, Z.Z. Li, X.L. Huang, H. Wang, X. Zhang, ACS Appl. Mater. Interfaces **8**, 34396–34404 (2016)
36. G.H. Chen, J. Yang, J.J. Tang, X.Y. Zhou, RSC Adv. **5**, 23067–23072 (2015)
37. Q. Li, X.G. Miao, C.X. Wang, L.W. Yin, J. Mater. Chem. A **3**, 21328–21336 (2015)
38. B. Wang, S.M. Li, X.Y. Wu, J.H. Liu, W.M. Tian, J. Chen, New J. Chem. **40**, 2259–2267 (2016)
39. H. Long, T.L. Shi, S.L. Jiang, S. Xi, R. Chen, S.Y. Liu, G.L. Liao, Z.R. Tang, J. Mater. Chem. A **2**, 3741–3748 (2014)
40. R.C. Jin, H. Jiang, Y.X. Sun, Y.Q. Ma, H.H. Li, G. Chen, Chem. Eng. J. **303**, 501–510 (2016)
41. G. Liu, K.F. Wang, X.S. Gao, D.Y. He, J.P. Li, Electrochim Acta **211**, 871–878 (2016)
42. J.A. Wang, G.R. Yang, L. Wang, W. Yan, J. Mater. Chem. A **4**, 8620–8629 (2016)
43. Z.L. Zhang, Y.J. Ji, J. Li, Q.Q. Tan, Z.Y. Zhong, F.B. Su, ACS Appl. Mater. Interfaces **7**, 6300–6309 (2015)
44. C.Z. Yuan, J.Y. Li, L.R. Hou, X.G. Zhang, L.F. Shen, X.W. Lou, Adv. Funct. Mater. **22**, 4592–4597 (2012)
45. F.C. Zheng, D.Q. Zhu, Q.W. Chen, ACS Appl. Mater. Interfaces **6**, 9256–9264 (2014)
46. J.F. Li, S.L. Xiong, Y.R. Liu, Z.C. Ju, Y.T. Qian, ACS Appl. Mater. Interfaces **5**, 981–988 (2013)

47. J.H. Zhong, A.L. Wang, G.R. Li, J.W. Wang, Y.N. Ou, Y.X. Tong, J. Mater. Chem. **22**, 5656–5665 (2012)

48. L.N. Qu, X.H. Hou, J.W. Mao, Q. Ru, S.J. Hu, X. Liu, K.H. Lam, RSC Adv. **6**, 96743–96751 (2016)

49. Y.L. Xiao, J.T. Zai, X.M. Li, Y. Gong, B. Li, Q.Y. Han, X.F. Qian, Nano. Energy **6**, 51–58 (2014)

50. W.M. Mei, J. Huang, L.P. Zhu, Z.Z. Ye, Y.J. Mai, J.P. Tu, J. Mater. Chem. **22**, 9315–9321 (2012)

51. Y.J. Chen, B.H. Qu, L.L. Hu, Z. Xu, Q.H. Li, T.H. Wang, Nanoscale **5**, 9812 (2013)

52. Y.D. Mo, Q. Ru, X. Song, L.Y. Guo, J.F. Chen, X.H. Hou, S.J. Hu, Carbon **109**, 616–623 (2016)

53. Y.S. Fu, Y.H. Wan, H. Xia, X. Wang, J. Power Sources **213**, 338–342 (2012)

54. M.V. Reddy, G.V.S. Rao, B.V.R. Chowdari, Chem. Rev. **113**, 5364–5457 (2013)

55. M.V. Reddy, G.V.S. Rao, B.V.R. Chowdari, J. Phys. Chem. C **111**, 11712–11720 (2007)

56. Y.J. Chen, J. Zhu, B.H. Qu, B.A. Lun, Z. Xu, Nano Energy **3**, 88–94 (2014)

57. M.V. Reddy, B.L.W. Wen, K.P. Loh, B.V.R. Chowdari, ACS Appl. Mater. Interfaces **5**, 7777–7785 (2013)

58. A.S. Hameed, H. Bahiraei, M.V. Reddy, M.Z. Shoushtari, J.J. Vittal, C.K. Ong, B.V.R. Chowdari, ACS Appl. Mater. Interfaces **6**, 10744–10753 (2014)

59. S.W. Kim, D.H. Seo, X.H. Ma, G. Ceder, K. Kang, Adv. Energy Mater. **2**, 710–721 (2012)

60. Y.C. Yang, X.M. Yang, Y. Zhang, H.S. Hou, M.J. Jing, Y.R. Zhu, L.B. Fang, Q.Y. Chen, X.B. Ji, J. Power Sources **282**, 358–367 (2015)

61. J.F. Chen, Q. Ru, Y.D. Mo, S.J. Hu, X.H. Hou, Phys. Chem. Chem. Phys. **18**, 18949–18957 (2016)

62. G. Huang, F.F. Zhang, X.C. Du, Y.L. Qin, D.M. Yin, L.M. Wang, ACS Nano **9**, 1592–1599 (2015)

63. L. Wang, J. Song, R.M. Qiao, L. Andrew Wray, M.A. Hossain, Y.D. Chuang, W.L. Yang, Y.H. Lu, D. Evans, J.J. Lee, S. Vail, X. Zhao, M. Nishijima, S. Kakimoto, J.B. Goodenough, J. Am. Chem. Soc. **137**, 2548–2554 (2015)

64. C. Yue, Y.J. Yu, S.B. Sun, X. He, B.B. Chen, W. Lin, B.B. Xu, M.S. Zheng, S.T. Wu, J. Li, J.Y. Kang, L.W. Lin, Adv. Funct. Mater. **25**, 1386–1392 (2015)